

Stratospheric Age-of-Air: Sensitivity to Finite Volume Remapping Algorithm

Clara Orbe ^{1,2}, Lawrence L. Takacs ³, Amal El Akkraoui ³,
Krzysztof Wargan ³, Andrea Molod ³

¹NASA Goddard Institute for Space Studies, New York, NY

²Department of Applied Physics and Applied Mathematics, Columbia University, New York, NY

³Global Modeling and Assimilation Office, NASA Goddard Space Flight Center, Greenbelt, MD

Key Points:

- In GEOS-5 the stratospheric mean age-of-air is sensitive to the remapping scheme used within the finite-volume dynamical core that controls how individual material surfaces are vertically interpolated back to standard pressure levels after each horizontal advection time step.
- This sensitivity in the age-of-air imprints not only on other idealized tracers, but also on several long-lived chemical trace gases (e.g., N₂O, CH₄).
- The age-of-air differences primarily reflect changes in resolved wave convergence over the Northern Hemisphere midlatitude stratosphere, which impact the strength of upwelling within the tropical lower stratosphere.

Corresponding author: =name=, =email address=

18 **Abstract**

19 Accurately modeling the large-scale transport of trace gases and aerosols is impor-
 20 tant for interpreting past (and projecting future) changes in atmospheric composition.
 21 Simulations of the stratospheric mean age-of-air continue to show persistent biases among
 22 chemistry climate models although the drivers of these biases are not well understood.
 23 Here we identify one key driver of simulated transport differences among various NASA
 24 Goddard Earth Observing System Version 5 (GEOS-5) candidate model versions that
 25 have been considered for the upcoming GEOS-5 Retrospective analysis for the 21st Cen-
 26 tury (GEOS-R21C). In particular, we use targeted model experiments aimed at disen-
 27 tangling the influence of recent model development updates, to show that the age-of-air
 28 is sensitive to the so-called “remapping” algorithm used within the finite-volume dynam-
 29 ical core that controls how individual material surfaces are vertically interpolated back
 30 to standard pressure levels after each horizontal advection time step. Differences in the
 31 age-of-air within the middle stratosphere (50 hPa) approach ~ 1 year over high latitudes
 32 - or about 30% climatological mean values - and imprint on a broad range of trace gases,
 33 including methane (CH_4) and nitrous oxide (N_2O). These transport sensitivities reflect,
 34 to first order, changes in the strength of tropical upwelling which are driven by changes
 35 in resolved wave convergence over northern midlatitudes as (critical lines of) wave prop-
 36 agation shift in latitude. Furthermore, we show that degradations in the performance
 37 of the age-of-air, stratospheric upwelling and zonal wind climate statistics derived from
 38 30-year-long atmosphere-only (AMIP) experiments, also translate to degraded skill in
 39 the analysis states used within data assimilation experiments. Our results strongly sup-
 40 port continued examination of the role of numerics in contributing to transport biases
 41 in composition modeling.

42 **Plain Language Summary**

43 TBD

44 **1 Introduction**

45 The chemical and radiative properties of the troposphere and lower stratosphere
 46 are strongly influenced by the stratosphere-troposphere exchange of mass and tracers (e.g.,
 47 Morgenstern and Carver (2001); Hegglin et al. (2006); Pan et al. (2007)). Properly sim-
 48 ulating the stratospheric circulation and its influence on atmospheric composition in earth
 49 system models is important for capturing past decadal trends in surface climate, par-
 50 ticularly in response to changes in Southern Hemisphere ozone depletion (e.g., Son et
 51 al. (2009); Polvani et al. (2011)). In the Northern Hemisphere (NH), the stratospheric
 52 circulation’s coupling to ozone could represent an important feedback on the climate’s
 53 response to future increases in greenhouse gases (GHGs), especially over the North At-
 54 lantic (e.g., Chiodo and Polvani (2019)). On shorter subseasonal timescales, stratospheric
 55 ozone changes associated with strong polar vortex states may also modulate Arctic sea
 56 level pressure and surface temperatures (e.g., Ivy et al. (2017); Oehrlein et al. (2020)),
 57 so much so that seasonal forecast systems employing prognostic ozone show increased
 58 signal-to-noise ratio in predictions of the North Atlantic Oscillation (B. M. Monge-Sanz
 59 et al. (2022)).

60 Key to properly ensuring a consistent and accurate representation of coupling be-
 61 tween the stratospheric dynamical circulation and atmospheric composition is ensuring
 62 that a model’s underlying transport circulation is well represented. To this end, much
 63 effort has been paid to developing and refining so-called “tracer-independent” metrics
 64 of transport (Holzer and Hall (2000)) such as the mean age-of-air (Hall and Plumb (1994))
 65 and to applying these measures to rigorously evaluate model transport characteristics

66 in chemistry climate models (CCMs) (e.g., Hall et al. (1999); Orbe et al. (2018); Dietmüller
67 et al. (2018); Abalos et al. (2020)).

68 While the assessment of CCMs participating in the SPARC Chemistry Climate Model
69 Validation (SPARC CCMVal) effort showed a marked improvement in simulated trans-
70 port characteristics relative to previous intercomparisons (J. Neu et al. (2010)), more re-
71 cent analysis of models participating in the SPARC Chemistry Climate Modeling Ini-
72 tiative (CCMI) (Eyring et al. (2013)) do not demonstrate any improvement (Dietmüller
73 et al. (2018), see their Figure 3). In particular, although some models produce mean age
74 values that agree well with observational estimates, the CCMI intermodel spread is $\sim 50\%$,
75 with models generally simulating transport that is too vigorous, relative to observations.
76 While documenting these transport differences among models is straightforward, under-
77 standing the drivers of this spread remains a key challenge and to this point there is no
78 consensus identifying a clear driver of simulated age biases among the current genera-
79 tion of CCMs.

80 A key challenge in identifying the drivers of age-of-air – and other stratospheric trans-
81 port – biases is that they reflect the time-integrated effects of advection by the residual
82 mean circulation and eddy diffusive mixing, or the quasi-random transport due to the
83 breaking of Rossby waves (e.g., Holton et al. (1995); Plumb (2002)). Given that the in-
84 fluences of mixing and advection are not easily separable, studies have come to differ-
85 ent conclusions about the drivers of age biases in models. In particular, the analysis of
86 the CCMVal models showed a strong correlation between the intermodel spread in the
87 age-of-air and lower stratospheric tropical upwelling, whereas Dietmüller et al. (2018)
88 argued that the age spread among the CCMI models was driven by differences in mix-
89 ing. While future attempts to further distinguish between these drivers of age biases us-
90 ing either simplified “leaky pipe” models (Plumb (1996); J. L. Neu and Plumb (1999))
91 or more complete measures of the transport circulation such as the “age spectrum” (e.g.,
92 Hall and Plumb (1994); Waugh and Hall (2002)) may prove enlightening, at present there
93 is no consensus on what is driving biases in the mean age in models.

94 A potential limitation of using multi-model intercomparisons to understand drivers
95 of age biases is that many aspects of model formulation can influence both stratospheric
96 (advective) upwelling and mixing. Thus, while intercomparisons are useful for identify-
97 ing common model biases, understanding the drivers of these biases is difficult absent
98 single model-based process studies. Among these, several aspects of model formulation
99 have been identified as influencing representations of the stratospheric mean age. As the
100 mean age is sensitive to vertical motion in the lowermost stratosphere, these include large
101 sensitivities to vertical resolution (Orbe et al. (2020)) and to spurious vertical mixing
102 either introduced in vertical coordinate transformations in offline chemical transport mod-
103 els (B. Monge-Sanz et al. (2007)) or through use of assimilated winds performed either
104 in offline (e.g., Legras et al. (2004)) or online data assimilation and “nudged” configu-
105 rations (e.g., Pawson et al. (2007); Orbe et al. (2017); Davis et al. (2022)). These age
106 sensitivities can be still further amplified, depending on whether or not parameterized
107 gravity waves are included (Eichinger et al. (2020)).

108 By comparison, sensitivities of the mean age to underlying tracer numerics have
109 been less well examined, although Eluszkiewicz et al. (2000) documented a large sensi-
110 tivity in age-of-air calculations to the choice of advection scheme. More recently, Gupta
111 et al. (2020) showed differences of $\sim 25\%$ in the age-of-air across identical experiments
112 performed using four different dynamical cores, especially between those using spectral
113 versus finite-volume schemes. The experiments employed in that study, however, were
114 highly idealized and it is not clear if the strong influence of tracer numerics that they
115 identified is also realized in more comprehensive model simulations, especially in the con-
116 text of model development as carried out in operational modeling centers.

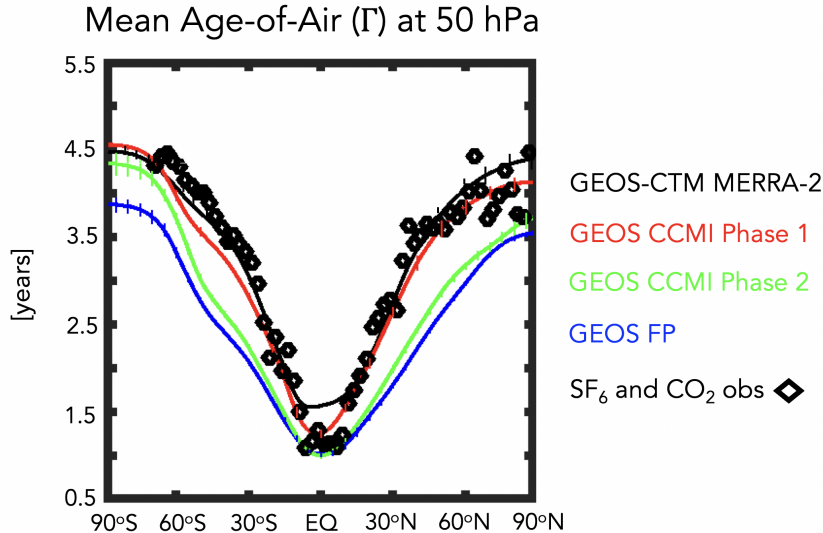


Figure 1. The 2000-2010 climatological annual mean meridional profile of the stratospheric mean age-of-air (Γ), evaluated at 50 hPa. Results from a GEOS-CTM integration constrained with MERRA-2 meteorological fields (black line) as well as free-running GEOS simulations using a model configuration for CCM1 Phase 1 (red line), CCM1 Phase 2 (green line) and a more recent GEOS-FP development tag (blue line) are shown. All simulations are constrained with the same (observed) historical sea surface temperatures. Diamonds correspond to SF_6 and CO_2 in situ based estimates of Γ from Boering1996stratospheric and Engel et al. (2009). Vertical dashed lines denote $\pm\sigma$, the standard deviation of Γ over 2000-2010, for each model simulation.

117 To this end, here we document the sensitivity of the stratospheric mean age in sev-
 118 eral recent versions of the NASA Goddard Earth Observing System Version 5 (GEOS-
 119 5) general circulation model (Molod et al., 2015) that represent different stages in model
 120 development since MERRA-2 (Gelaro et al. (2017)). Our focus on transport evaluation
 121 is in wake of the upcoming release of the GEOS-5 Retrospective analysis for the 21st Cen-
 122 tury (GEOS-R21C), which will serve as an intermediate reanalysis between MERRA-
 123 2 and MERRA-3 (~ 2025). As GEOS-R21C will be used to drive an off-line chemistry
 124 reanalysis (GEOS-R21C-Chem) it is imperative that it produces a credible representa-
 125 tion of transport processes.

126 In particular, in the process of evaluating candidate systems for GEOS-R21C it was
 127 noted that the mean age was ~ 1 younger than the values produced in the model ver-
 128 sion used to produce MERRA-2 (Figure 1). The model versions shown in Figure 1 re-
 129 flect more than 10 years’ worth of accumulated changes in model development, most no-
 130 tably changes in radiation, parameterized convection and, as we focus on here, changes
 131 in the algorithm used to transform advected fields from Lagrangian levels to fixed pres-
 132 sure levels after each horizontal advection time step. We show that slight modifications
 133 in this so-called “remapping” algorithm are the primary driver of the age-of-air degra-
 134 dation exhibited in recent GEOS-R21C candidate model versions, a result which may
 135 have broader implications for other general circulation models using finite volume (FV)
 136 dynamical cores. We begin by discussing methods in Section 2 and present key results
 137 and conclusions in Sections 3 and 4, respectively.

2 Methods

2.1 Model Configurations

Here we present results from several versions of GEOS-5 spanning MERRA-2 to more recent candidates for GEOS-R21C. Among these model versions, a subset are more “official” as they have been documented and/or employed in recent model intercomparisons and are highlighted in Figure 1. In particular, these include an intermediary model version that was used in Phase 1 of CCMI and documented in Orbe et al. (2017), marked in the red line. In addition, a later version that was used in the CCMI Phase 2 simulations (correspondence with Michael Manyin) is shown in the green line.

We begin by comparing 10-year (2000-2010) climatological mean zonally averaged age-of-air profiles at 50 hPa across this subset of model versions, derived from 30-year long atmosphere-only (AMIP) integrations constrained with observed sea surface temperatures (Figure 1). First, we note that the profiles for the CCMI Phase 1 version of the model (blue line) are very close to observations (black stars), consistent with the “GEOSCCM” documented age characteristics reported in Dietmüller et al. (2018) (see their Figure 3). In addition, while passive tracers were not integrated within MERRA-2, results using the GEOS chemistry transport model (GEOS-CTM, Kouatchou et al. (2015)) constrained with MERRA-2 meteorological fields (black line) also exhibits good agreement with observed values. This good agreement between the CTM-generated age-of-air and the observations is consistent with results from a previous GEOS-CTM simulation (constrained with MERRA) that was documented in Orbe et al. (2017).

Moving to more recent development versions of the model (green and blue lines), however, reveals a reduction in the mean age by ~ 1 year over both southern and northern high extratropical latitudes, or a decrease of $\sim 20\text{-}30\%$ relative to MERRA-2. As discussed earlier, the green line refers to the CCMI Phase 2 model version, whereas the blue line refers to an undocumented candidate version that corresponds best to a model configuration similar to what is used in the GEOS forward processing (FP) numerical weather prediction system (*As of which date? Ask Amal.*). Note that this decrease in the age in both model versions is statistically significant, relative to internal variability (vertical bars on solid lines).

As there were numerous development updates in the model that occurred since MERRA-2, after discussing the model configurations highlighted in Figure 1 in Section 3.1, we then perform targeted experiments oriented at successively undoing various changes that were made to the model since MERRA-2 (Section 3.2). Among those aspects most likely impacting the stratospheric transport circulation, these include updates to the radiation scheme, moving from Chou and Suarez (1994) in the shortwave and Chou (1990, 1992) in the longwave to the Rapid Radiative Transfer Model for GCMS (RRTGM; Iacono et al. (2008)).

In addition to the radiation changes, another more consequential model development was made to the handling of the remapping algorithm within the model’s finite-volume (FV) dynamical core. In particular, vertical motion is realized through the Lagrangian transport of the “floating” vertical coordinate such that after each horizontal advection step the individual material surfaces are vertically interpolated back to standard pressure levels through FV’s so-called “REMAP” algorithm. There are various user-defined parameters and decisions that are made within this interpolation process.

First, the vertical remapping algorithm in its current implementation involves 1) computing total energy ($TE = C_p T + K + \Phi$) on the input grid; 2) fitting piecewise parabolic functions to layer-mean values of TE, u, v and tracers; 3) producing new layer-mean values by integrating functions between edges of the output grid and 4) constructing a “remapped” temperature profile via $T = (TE - K - \Phi)/C_p$. Note that T, u, v, C_p , K and Φ correspond to temperature, zonal wind, meridional wind, specific heat capacity and kinetic and po-

Table 1. Finite Volume Remapping Algorithm: The two versions examined in this study control how individual material surfaces are vertically interpolated back to standard pressure levels. REMAP Options 2 and 1 corresponds to the configurations used in more recent (green and blue lines, Figure 1) and older (red and black lines, Figure 1) model configurations, respectively. Here T , u , v , C_p , K and Φ correspond to temperature, zonal wind, meridional wind, specific heat capacity and kinetic and potential energy, respectively.

Step	REMAP Option 2 (CTRL)	REMAP Option 1 (MERRA-2)
1	compute $TE = C_p T + K + \Phi$ on input grid	compute $TE = C_p T + K + \Phi$ on input grid
2	Fit PPM functions to layer-mean TE , u , v and tracers	Fit PPM functions to layer-mean u , v and tracers
3	Integrate functions between output grid edges to produce new layer- mean TE , u , v and tracers	Integrate functions between output grid edges to produce new layer- mean u , v and tracers
4	Construct “remapped” T via $T = (TE - K - \Phi)/C_p$	Calculate TE at new mid-layer pressures using cubic interpolation and a-posteriori integral conservation
5	n/a	Construct “remapped” T via $T = (TE - K - \Phi)/C_p$

189 tential energy, respectively. This implementation setup is consistent with what is cur-
 190 rently being used in most recent model versions (i.e. blue and green lines, Figure 1) and
 191 hereafter is referred to as REMAP Option 2 (Table 1, left). The alternative version –
 192 which best mimics what was used in MERRA-2 – involves two changes to this procedure
 193 and is hereafter referred to as REMAP Option 1 (Table 1, right; red line in Figure 1).
 194 First step 2) is performed only for u , v and tracers (not TE). Second, an additional step
 195 between 3) and 4) is added which involves calculating TE at new mid-layer pressures us-
 196 ing cubic interpolation and a posteriori ensuring integral conservation.

197 It is worth noting other important model development changes that occurred re-
 198 lated to the parameterization of deep convection (Grell and Freitas (2014); Freitas et al.
 199 (2018)) which could, potentially, have an indirect impact on the stratospheric circula-
 200 tion through their influence on wave propagation into the stratosphere. As we show, how-
 201 ever, while these have a substantial impacts upon their incorporation in a nonhydrostatic
 202 version of the model on characteristics like the diurnal cycle of precipitation (Arnold et
 203 al. (2020)) and on convective transport within the troposphere (Freitas et al. (2020)),
 204 their indirect influence on the stratosphere is less impactful.

205 To this end, in order to investigate the drivers of the differences illustrated in Fig-
 206 ure 1 we perform targeted model experiments aimed at further disentangling all of these
 207 development changes (Table 2). First, we begin by defining a control experiment (CTRL;
 208 Table 2, row 1), which best corresponds to the blue line shown in Figure 1. Then we de-
 209 fine three new experiments based off this control that are used to distinguish between
 210 the age changes resulting from changes in radiation versus changes in the handling of
 211 the REMAP algorithm (Section 3.2.1). Specifically, these include experiments in which
 212 we revert back from RRTMG to Chou and Suarez (1994) in the shortwave (CSRAD; Ta-
 213 ble 2, row 2), b) revert back to the MERRA-2 REMAP approach (i.e. REMAP Option
 214 1) (M2REMAP; Table 2, row 3) and c) combine these two changes (CSRAD+M2REMAP;
 215 Table 2, row 4). Note that we have also have performed experiments in which RRTMG

Table 2. GEOS Model Experiments: Targeted GEOS-5 model experiments based off a control experiment (row 1) were carried out to identify the influence of radiation (row 2) and the FV remapping algorithm changes since MERRA-2 (row 3), as well as their combined influence (row 4). Sensitivities within the FV remapping algorithm were further explored with respect to the order of the interpolation to pressure levels (rows 5-9). Experiments in rows 1-7 are 30-year-long AMIPS used for climate statistic evaluation, whereas rows 8-9 are 1-year-long DAS runs used for evaluation of the analysis state.

Experiment Name	Configuration Change	Experiment Type
CTRL	Control, REMAP Option 2	AMIP (30 yrs.)
CSRAD	Chou-Suarez (1994) Shortwave (SW) Radiation	AMIP (30 yrs.)
M2REMAP	MERRA-2 REMAP Option 1 (cubic)	AMIP (30 yrs.)
CSRAD+M2REMAP	Chou-Suarez (1994) SW + REMAP Option 1 (cubic)	AMIP (30 yrs.)
LINEAR	MERRA-2 REMAP Option 1 (linear)	AMIP (30 yrs.)
QUADRATIC	MERRA-2 REMAP Option 1 (quadratic)	AMIP (30 yrs.)
CUBIC	MERRA-2 REMAP Option 1 (cubic)	AMIP (30 yrs.)
CTRL-DAS	Control, REMAP Option 2	DAS (1 yr.)
CUBIC-DAS	MERRA-2 REMAP Option 1 (cubic)	DAS (1 yr.)

216 is reverted back to Chou (1990); Chou and Suarez (1994) in the longwave (not shown),
217 but these changes are less impactful, compared to the shortwave changes.

218 As we will show, the M2REMAP experiment produces the largest changes in age-
219 of-air and we thus focus the remainder of our investigation (Section 3.2.2) on examin-
220 ing a clean set of experiments in which only the interpolation occurring between steps
221 3) and 4) within REMAP Option 1 is altered. Specifically, we perform three experiments
222 that are all based off the CTRL configuration and revert back to the REMAP Option
223 1. The difference between them is that the calculation of TE at the mid-layer pressure
224 levels is performed either using a linear (LINEAR; Table 1, row 5), quadratic
225 (QUADRATIC; Table 1, row 6) or cubic interpolation (CUBIC; Table 1, row 7), with
226 the latter corresponding to the approach that was used in MERRA-2. We note that, while
227 the LINEAR and QUADRATIC experiments do not actually correspond to any of the
228 development tags shown in Figure 1, they highlight the large sensitivity of the mean age
229 to otherwise innocuous seeming changes in the interpolation scheme. We also show that
230 they provide further support for the relationship between upwelling strength and strato-
231 spheric mean age as realized in GEOS.

232 Finally, in all experiments using REMAP Option 1 (i.e. M2REMAP, CSRAD+
233 M2REMAP, LINEAR, QUADRATIC, CUBIC) additional modifications to the diver-
234 gence damping coefficients were used so as to ensure best consistency with what was used
235 in MERRA-2. As they only differ in this single respect, these experiments are therefore
236 useful for cleanly isolating the impacts of changes in the interpolation scheme. Specif-
237 ically, these include changes to the number of layers for vertical subgrid mixing, the DAS
238 coefficient for barotropic mode damping, the use of 2nd vs. 6th order divergence damp-
239 ing and the strength of the divergence damping coefficients.

240

2.2 Analysis Approach

241

2.2.1 Stratospheric Circulation and Transport Diagnostics

242

243

244

245

246

247

248

249

250

251

252

253

254

255

256

To diagnose the transport circulation we focus primarily on the age-of-air (Hall and Plumb (1994)). This is inferred from an idealized global “clock” or ideal age tracer (Γ) (Thiele and Sarmiento (1990)) that is defined with respect to all grid points in the first model level. Initially, the ideal age tracer is set to zero throughout the troposphere and thereafter held to zero over the entire Earth’s surface, subject to a constant aging of 1 year/year throughout the atmosphere. We present here the statistically stationary (equilibrated) value of $\Gamma(r)$, which is equal to the average time since the air at a location r in the stratosphere last contacted the Earth’s surface. In addition to the mean age, we also show results from an idealized e90 tracer that is uniformly emitted over the entire surface layer and decays exponentially at a rate of 90 days⁻¹ such that concentrations greater than 125 ppb and less than 50 ppb tend to reside in the lower troposphere and stratosphere, respectively (Prather et al. (2011)). As this tracer features strong near-tropopause gradients and takes significantly less time to equilibrate, compared to the mean age, it is useful for evaluating stratosphere-troposphere-exchange and transport within the upper troposphere/lower stratosphere (Abalos et al. (2017, 2020)).

257

258

259

260

261

262

263

In addition to the idealized tracers, we also evaluate the impacts of the age changes on real trace gas distributions. Two of the experiments shown here were run with full interactive chemistry and correspond to the two CCM1 (Phase 1 and Phase 2) integrations (red and green lines, Figure 1), which both employed the same Global Modeling Initiative (GMI) chemical mechanism (Strahan et al. (2013)). Results from these experiments show the imprint of the age-of-air changes on nitrous oxide (N₂O) and methane (CH₄).

264

265

266

267

268

269

270

271

272

273

274

275

276

As we show in Section 3, the changes in age-of-air across the different model versions are strongly tethered to changes in the advective component of the circulation, which we quantify using the Transformed Eulerian Mean (TEM) framework. Thus, in addition to more standard Eulerian metrics of the circulation (e.g., zonal winds and temperatures), we also examine the TEM estimate of the Lagrangian transport of mass by the circulation, which is far more relevant to constituent transport. In particular, we focus on the vertical component of the TEM residual velocity, defined as $\bar{w}^* = \bar{w} + \frac{\partial(\psi \cos \phi)}{\partial \phi}$, where $\psi = \overline{v'\theta'}/\frac{\partial \bar{\theta}}{\partial p}$ is the eddy stream function, θ refers to potential temperature and overbars and primes denote zonal means and deviations therefrom, respectively (Andrews et al. (1987)). In addition, in order to interpret the response in w^* we examine the Eliassen-Palm flux divergence ($\nabla \cdot F$), whose horizontal ($F(\phi)$) and vertical ($F(p)$) components are respectively defined as $F(\phi) = \overline{\cos \phi [\frac{\partial u}{\partial p} \psi - u'v']}$ and $F(p) = \overline{\cos \phi [f - \frac{\partial u \cos \phi}{\partial \phi}] \psi - u'\omega'}$.

277

2.2.2 Experimental Setup

278

279

280

281

282

283

284

285

286

We begin our analysis by interpreting the results shown in Figure 1, which are all based on AMIPs performed over the period Dec 1985 – Feb 2015 (**Check with Larry exact years**). As these runs represent more “official” model tags they are performed at different horizontal resolutions (indicated in the figure caption **TO DO**). A clean/meaningful analysis of this set of runs is therefore hampered not only by the model development differences between them, but also by resolution differences. Nonetheless, they present an important motivation for the experiments that follow. They also indirectly highlight how other development changes that occurred (to convection, for example) were less consequential in terms of their impacts on the stratospheric circulation.

287

288

Given the limitations of the experiments highlighted in Figure 1, we focus the bulk of our analysis on the model configurations listed in Table 2. For these model runs cli-

289 climatological AMIPs were carried at a cubed sphere C180 (approximately half-degree) res-
 290 lution and used to infer the climate characteristics of the different model configurations.
 291 For a subset of these experiments (Table 2, rows 5-9) integrations were also carried out
 292 at C360 horizontal resolution. All integrations carry the same idealized passive tracer
 293 package (including the e90 and Γ tracers) that was described in Orbe et al. (2017).

294 In addition to AMIPs we also include results from so-called “EMIPs” which were
 295 also run at C180 and consist of performing ensembles of 3-month-long integrations ini-
 296 tialized on December 1 of each year between 1985 and 2015 (Larry, is this correct?). As
 297 we show, the December-January-February (DJF) climatological mean statistics derived
 298 from EMIP experiments of various climate metrics converge to the statics of the corre-
 299 sponding AMIP runs using the same model configurations. In particular, we find excel-
 300 lent agreement between the vertical profile of w^* , averaged over 1985-2015 and between
 301 the tropical turnaround latitudes, deduced from AMIP and EMIP experiments run us-
 302 ing one of the model tags described herein (corresponding to the blue line in Figure 1)
 303 (Appendix Figure 1). This somewhat incidental finding, represents, to the best of our
 304 knowledge, the first time that this result has been documented for the stratospheric met-
 305 rics considered in this study. Furthermore, as EMIPs present a much more computationally
 306 efficient alternative to running AMIPs, this approach was used to quickly ascertain
 307 the impacts of the changes documented in Table 2. We note, however, that this approach
 308 is not appropriate for evaluating the time-integrated transport characteristics reflected
 309 in the age-of-air. To this end, we show results from both AMIP and EMIP experiments.

310 Finally, in addition to examining the climate statistics of the different model con-
 311 figurations we also inquire into implications for the analyzed atmospheric states from data
 312 assimilation for a subset of the experiments (Table 2, rows 8-9). Specifically, we exam-
 313 ine the root-mean-square error of various climate fields (Amal, need description of rel-
 314 evant metrics/analysis). This evaluation is important given that in GEOS-R21C any un-
 315 derlying model biases will be partly ameliorated through replaying of the model state
 316 to the analysis. Assessing the impact of reduced biases from the free-running model for
 317 the analysis state, is therefore important for informing the development of GEOS-R21C.

318 2.3 Observations and Reanalyses

319 While our focus is on interpreting and understanding the behavior across the dif-
 320 ferent model versions, we incorporate observations to provide context, although we do
 321 not present an exhaustive evaluation of the model’s transport characteristics (for that
 322 see earlier studies including Orbe et al. (2017, 2018)). For the circulation diagnostics all
 323 comparisons are made relative to MERRA-2, although similar comparisons against ERA-
 324 5 have also been made (not shown) and reveal a similar picture.

325 As the tracers are not directly integrated in MERRA-2 (with the exception of ozone),
 326 we compare against independent observational estimates. For the mean age we first com-
 327 pare simulated meridional age profiles at 50 hPa with values derived from in situ aircraft
 328 measurements of carbon dioxide (CO_2), averaged in 2.5 degree latitude bins over the al-
 329 titude range 19.5 to 21.5 km (Boering et al. (1996), see also Figure 5 in Hall et al. (1999)).

330 We also briefly evaluate impacts of transport biases on the simulated trace gas dis-
 331 tributions for the CCM1 Phase 1 and 2 experiments. The simulated fields of methane
 332 (CH_4) are compared with the climatologies derived for 1991–2002 from the Halogen Oc-
 333 cultation Experiment (HALOE) on board the Upper Atmosphere Research Satellite (UARS)
 334 (Grooß and Russell III (2005)). Comparisons of simulated nitrous oxide (N_2O) are made
 335 against 2005–2015 climatologies derived from the Microwave Limb Sounder (MLS) on
 336 the Earth Observing System (EOS) Aura satellite. We use the 190-GHz retrieval from
 337 Version 4.2 because the 640-GHz data set ends in summer 2013 due to the failure of the
 338 N_2O primary band.

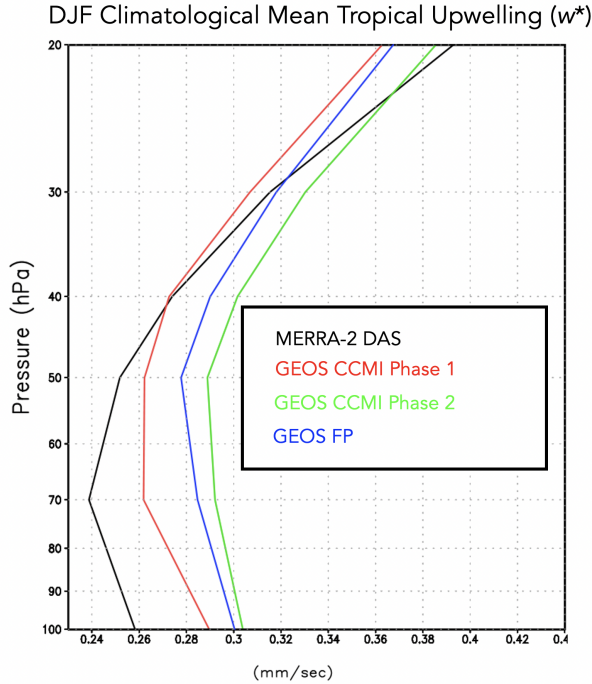


Figure 2. The DJF 1985-1994 (ideally would include years 1994-2015) climatological mean vertical residual mean velocity, w^* , averaged between the turnaround latitudes for GEOS model configurations corresponding to the CCM1 Phase 1 (red) and Phase 2 (green) submissions and to GEOS-FP (blue). MERRA-2 is shown in black.

339 3 Results

340 3.1 Reduction in Stratospheric Mean Age Since MERRA-2

341 We begin by interpreting the reduction in mean age exhibited in more recent model
 342 versions in terms of changes in the strength of upwelling associated with the Brewer-Dobson
 343 circulation. In particular, we find that the reductions in Γ (Figure 1) are consistent with
 344 increases in the strength of lower stratospheric tropical upwelling, with w^* becoming pro-
 345 gressively stronger in more recent model tags, relative to MERRA-2 (Figure 2). Though
 346 perhaps naive, this relationship between lower stratospheric upwelling and the mean age
 347 is consistent with the long-term behavior of Γ inferred from both historical and projected
 348 future climate simulations (Butchart et al. (2010); Abalos et al. (2021)). A strong re-
 349 lationship between the strength of lower stratospheric ascent and the mean age was also
 350 shown to hold in the CCMVal models (see Fig. 5.20 in J. Neu et al. (2010)). Neverthe-
 351 less, it is important to note that a clear relationship between w^* and Γ is not a priori
 352 expected, as the age-of-air is also known to be very sensitive to mixing, which may be
 353 important in interpreting differences among the CCM1 Phase 1 models (Dietmüller et
 354 al. (2018)).

355 The differences in w^* highlighted in Figure 2 are associated with enhanced Eliassen-
 356 Palm flux convergence over NH midlatitudes (Figure 3), relative to MERRA-2. Increased
 357 wave convergence is evident not only within the subtropical lower stratosphere ($< 30^\circ\text{N}$,
 358 50-100 hPa) but also over higher latitudes and altitudes ($\sim 40^\circ\text{-}70^\circ\text{N}$, 20-50 hPa). The
 359 fact that differences in extratropical wave convergence imprint on tropical upwelling is
 360 consistent with our understanding of the so-called “downward control” principal (Haynes

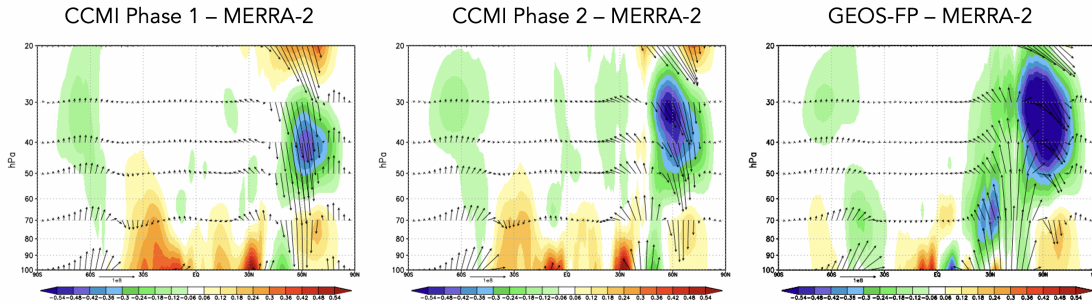
DJF Climatological Mean Eliassen-Palm Flux Divergence ($\nabla \cdot \mathbf{F}$)

Figure 3. Colors shown anomalies in the DJF climatological mean Eliassen-Palm (EP) flux divergence between the CCMI Phase 1 (left), CCMI Phase 2 (middle) and GEOS-FP (right) model versions, relative to MERRA-2. Arrows denote anomalies in the vertical and meridional EP flux vectors (relative to MERRA-2).

et al. (1991)). In particular, the strength of the residual mean streamfunction (Ψ^*) is, via downward control, directly related to the vertically integrated eddy-induced total zonal force above that level and has contributions both from the (resolved wave) Eliassen-Palm flux divergence (Figure 3) as well as parameterized waves (not shown). The tropical upward mass flux – defined as $\Psi_{\max}^* - \Psi_{\min}^*$ evaluated at the turnaround latitudes (e.g. Rosenlof (1995)) – is therefore directly dependent on the wave forcing aloft. Over extratropical latitudes, the zonal force associated with wave convergence will be associated with downwelling at high latitudes that will, through mass balance, necessarily be accompanied by enhanced upwelling in the tropics. This indirect impact of higher latitude wave drag can be seen in our simulations (Appendix Figure 2, [Ask Lary to make](#)), which show enhanced downwelling over the NH polar region that is consistent with enhanced upwelling over the tropics.

While the reduction in Γ (Figure 1) of $\sim 30\%$ at 50 hPa is significant, it is neither clear if this change is representative of other altitudes within the stratosphere nor how this age bias imprints on real chemical species. To this end, we begin by comparing the full latitude-pressure distribution of changes in Γ and another passive tracer (e90) (Figure 4) between the CCMI Phase 1 and Phase 2 model configurations (red and green lines, Figure 1). In particular, we find that the changes in both passive tracers – large reductions in Γ within both hemispheres (Fig. 4, top right) and increased values of e90 within the lower stratosphere (Fig. 4, bottom right) – are reflective of an overall increase in the strength of the transport circulation. This is highlighted in the CCMI Phase 2 – 1 model differences for the passive tracer distributions (Fig. 4, right panels) which are shown in the absence of robust observational constraints of Γ at higher altitudes (or any observational constraints for e90, for that matter). The reduced/increased stratospheric burdens of the age and e90 tracers are consistent with stronger upwelling in the CCMI Phase 2 model configuration (Figure 2).

While the observational constraints on Γ presented in Figure 1 and the departure of w^* away from MERRA-2 suggest that transport properties of the newer model configurations are moving in the wrong direction, it is relevant to ask whether or not the trace gas satellite measurements also support this conclusion. Indeed, comparisons with observations show larger biases in N_2O (Fig. 5, top panels) and CH_4 (Fig. 5, bottom panels), increasing from 10% to 30% in the CCMI Phase 2 model configuration, depending

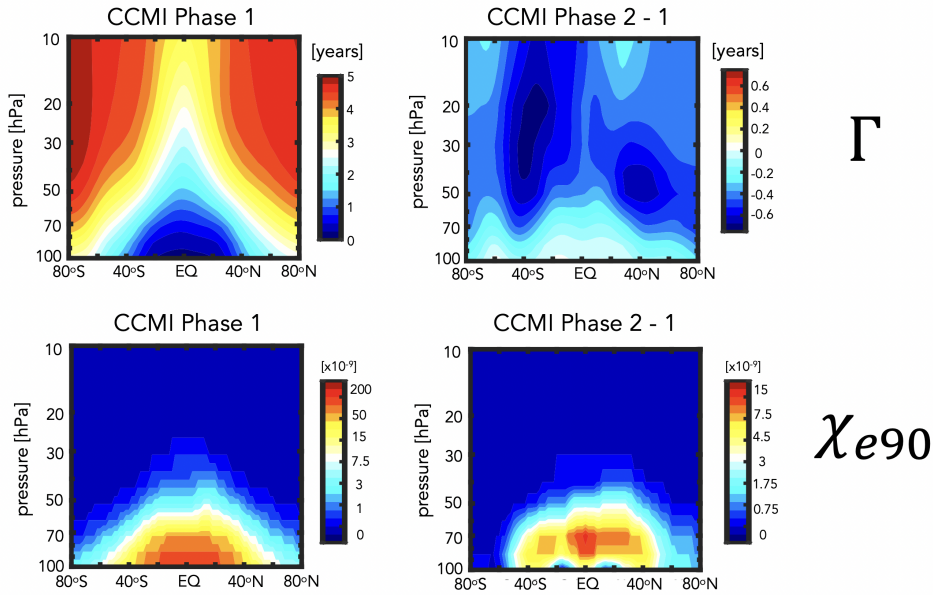


Figure 4. The climatological mean (2000-2010) distribution of the mean age-of-air (Γ) (left, top) and e90 idealized tracers (left, bottom) for the CCMI Phase 1 model configuration. Climatological differences between the CCMI Phase 2 and Phase 1 model configurations are shown in the left panels. Note that a nonlinear colorbar has been used in the e90 subplots.

393 on the species. The patterns of these biases are generally consistent with the biases in
 394 the mean age (Fig. 4), suggesting a strong link between the tracers. Recall that the same
 395 chemistry mechanism is used in both CCMI Phase 1 and 2 simulations.

396 The fact that the mean age changes have a significant imprint on the simulated trace
 397 gases is consequential for the GEOS-RC21 system. However, the configurations shown
 398 in Fig. 1-5 differ in many respects (physics, resolution, radiation, FV remapping algo-
 399 rithm) and it is difficult to meaningfully interpret what is driving the changes in w^* (and
 400 the tracers). We therefore move next to the targeted model experiments (Table 2) in or-
 401 der to interpret the model development steps that resulted in these transport circula-
 402 tion changes.

403 3.2 Identifying Drivers of Upwelling and Tracer Changes Since 404 MERRA-2

405 3.2.1 Radiation versus REMAP Algorithm

406 As discussed in Section 2, among the model changes that were made since MERRA-
 407 2, the changes in radiation and the FV remapping algorithm are most likely to directly
 408 have impacted the stratospheric circulation. We therefore begin by assessing which of
 409 these changes dominates the decreases in Γ shown in Figure 1.

410 Figure 6 shows the distribution of Γ for experiments in which the shortwave radi-
 411 ation and REMAP updates since MERRA-2 have successively been undone. Relative to
 412 the control experiment (CTRL; Table 2, row 1), the reversion back to Chou (1992) in
 413 the shortwave results in an increase in the mean age of ~ 0.5 years throughout the strato-
 414 sphere (CSRAD; Table 2, row 2). Though significant, this change in Γ is smaller than
 415 the change that results from reverting back to REMAP Option 1 (M2REMAP; Table

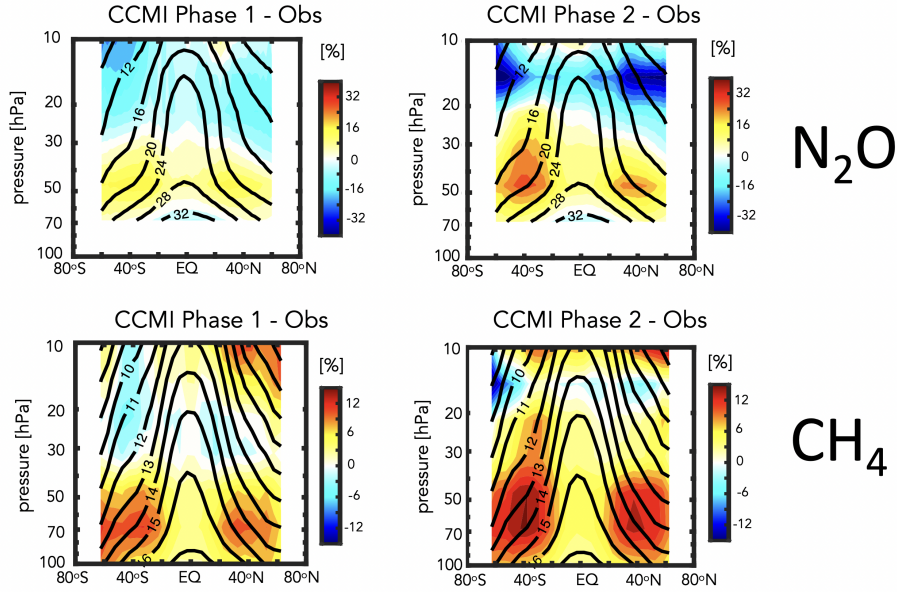


Figure 5. Colors shown anomalies in the simulated distributions of nitrous oxide (N_2O) (top) and methane (CH_4) (bottom), relative to the MLS and HALOE observed values, respectively, for the CCMI Phase 1 (left) and Phase 2 (right) GEOS model configurations. Climatological mean observed values are shown in the black contours.

416 1; row 3), in which the mean age increases by ~ 1 year. The combined impacts of both
 417 changes (CSRAD+M2REMAP; Table 1 row 4) is roughly linear, with age values of \sim
 418 5.5 years over high latitudes at 50 hPa, consistent with the values simulated by the GEOS-
 419 CTM MERRA-2 integration (black line in Figure 1) and with the CCMI Phase-1 ver-
 420 sion of the model (red line, Figure 1).

421 Next we ask if the behavior of Γ exhibited in Figure 6 can be interpreted in terms
 422 of changes in the strength of lower stratospheric tropical upwelling and extratropical wave
 423 convergence, as our previous analysis of the CCMI experiments suggested. Indeed, Fig-
 424 ure 7 shows that values of upwelling decrease in the CSRAD and M2REMAP experiments,
 425 with larger decreases in the latter, relative to the CTRL integration. The increase in up-
 426 welling resulting from both changes (CSRAD+M2REMAP) is still larger, consistent with
 427 the larger age decreases in that experiment. This change in the behavior of w^* within
 428 the tropical stratosphere can be interpreted in terms of changes in the Eliassen Palm flux
 429 convergence over NH midlatitudes (not shown, **should consider adding this as a figure**),
 430 which features smaller values in the CSRAD, M2REMAP (and CSRAD+MSREMAP)
 431 experiments. Note that our examination of the changes in w^* are derived from EMIP
 432 integrations, which we showed previously converge (for DJF) to the statistics derived from
 433 corresponding AMIP experiments.

434 3.2.2 FV REMAP Algorithm: Sensitivity of Climate Statistics

435 Having shown in the previous section that the largest changes in the mean age and
 436 lower stratospheric upwelling were realized through the reversion back to REMAP Op-
 437 tion 1, we now investigate further the sensitivity of the transport circulation to the choice
 438 of remapping interpolation scheme. In particular, we compare simulations in which to-
 439 tal energy is calculated at new mid-layer pressures using cubic, quadratic and linear in-

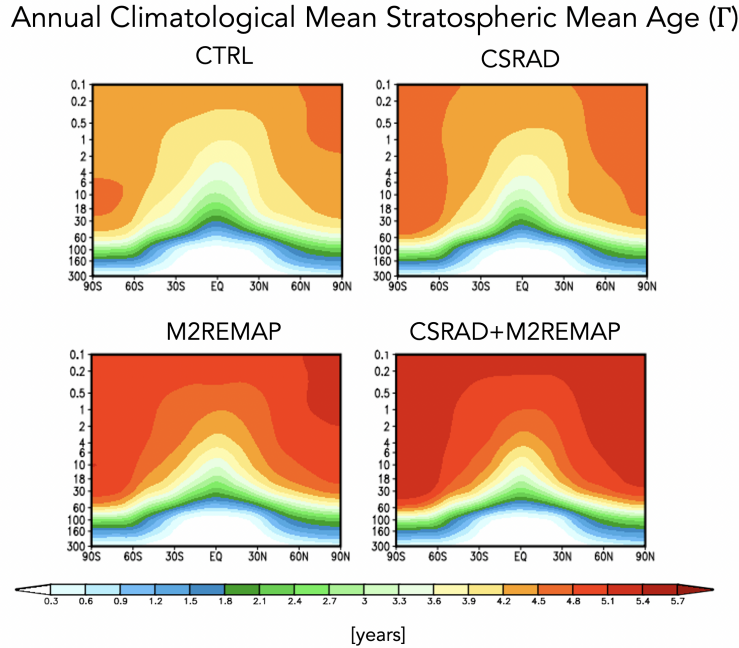


Figure 6. Colors show the simulated 2000-2010 climatological annual mean distributions of the mean age-of-air (Γ) for the CTRL (top left; Table 1, row 1), CSRAD (top right; Table 1, row 2), M2REMAP (bottom left; Table 1, row 3) and combined CSRAD+M2REMAP (bottom right; Table 1, row 4) experiments.

440 terpolation prior to the aposterior integral conservation (Table 2, rows 5-7). In addition,
 441 in this section we seek to understand how the changes in the Eliassen-Palm flux conver-
 442 gence over NH midlatitudes arise via analysis of the large-scale wind structure.

443 Figure 8 (left panels) shows a clear sensitivity in tropical upwelling to the choice
 444 of interpolation scheme, with w^* progressively increasing in strength moving from the
 445 CUBIC to QUADRATIC to LINEAR schemes. This sensitivity is robust across horizon-
 446 tal resolutions as the same suite of experiments performed at C360 exhibit the same sensi-
 447 tivity (Fig. 8, right panels). While no current model tag actually employs a linear scheme
 448 (the control simulation, rather uses a piecewise parabolic method and is delineated in
 449 the cyan line), this suite of experiments highlights the strong sensitivity to choice of in-
 450 terpolation scheme within the remapping algorithm, heretofore unreported in the liter-
 451 ature. Furthermore, as we show next, this clean set of experiments allow us to inquire
 452 mechanistically into the processes that are driving the changes in wave convergence over
 453 midlatitudes, unencumbered by differences in horizontal resolution, physics, etc.

454 Consistent with our expectations based on the analysis of the previous experiments,
 455 the drivers of the changes in w^* are related to increased wave convergence moving from
 456 the CUBIC to QUADRATIC to LINEAR schemes (Figure 9). Unlike in the previous sec-
 457 tions, however, we exploit the fact that these experiments only differ with respect to the
 458 interpolation scheme to further inquire into the drivers of the wave convergence changes.
 459 To this end, Figure 10 compares profiles of the zonal mean zonal wind between the CU-
 460 BIC, QUADRATIC and LINEAR experiments, averaged over the region of enhanced wave
 461 convergence (i.e. 20°N-60°N). The experiments featuring stronger wave convergence (LIN-
 462 EAR and QUADRATIC) are also simulations with stronger zonal winds, relative to MERRA-
 463 2, especially above 70 hPa. This change in winds occurs at both C180 (Fig. 10, left panel)
 464 and C360 (Fig. 10, right panel) resolutions.

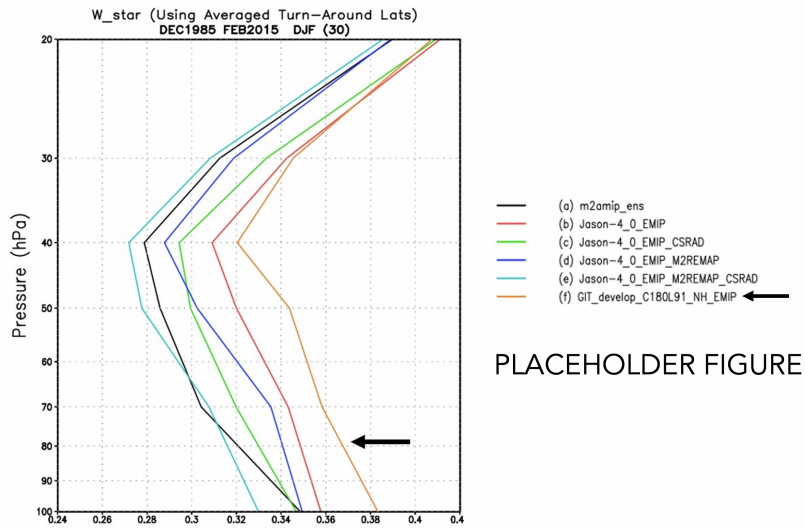


Figure 7. The DJF climatological mean vertical residual mean velocity, w^* , averaged between the turnaround latitudes for the CTRL (red line; Table 2, row 1), CSRAD (green line; Table 2, row 2), M2REMAP (blue line; Table 2, row 3) and combined CSRAD+M2REMAP (cyan line; Table 2, row 4) experiments. MERRA-2 is shown in black. **This figure still needs to be refined.**

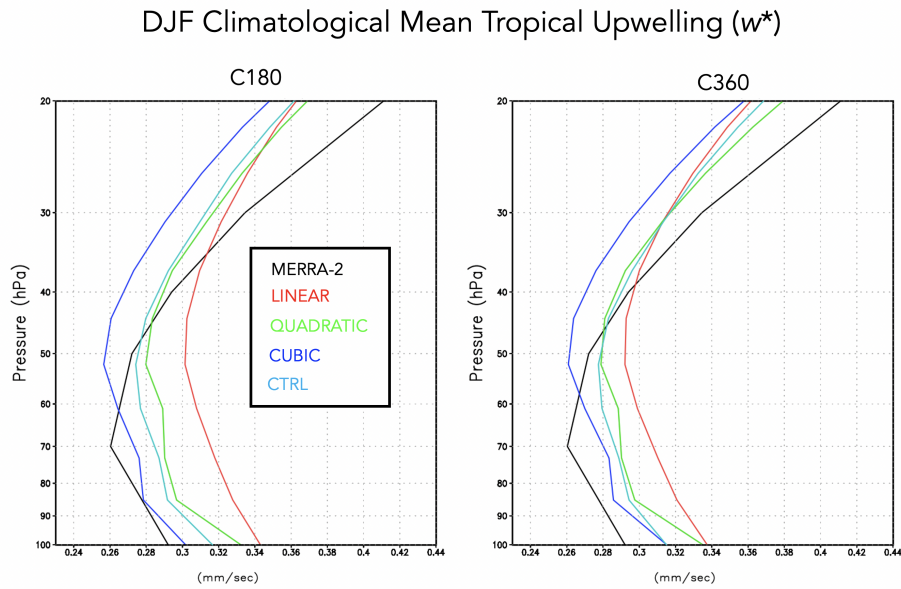


Figure 8. The DJF climatological mean vertical residual mean velocity, w^* , averaged between the turnaround latitudes for the CTRL (cyan line; Table 2, row 1), LINEAR (green line; Table 2, row 5), QUADRATIC (blue line; Table 2, row 6) and CUBIC (cyan line; Table 2, row 7) experiments. MERRA-2 is shown in black.

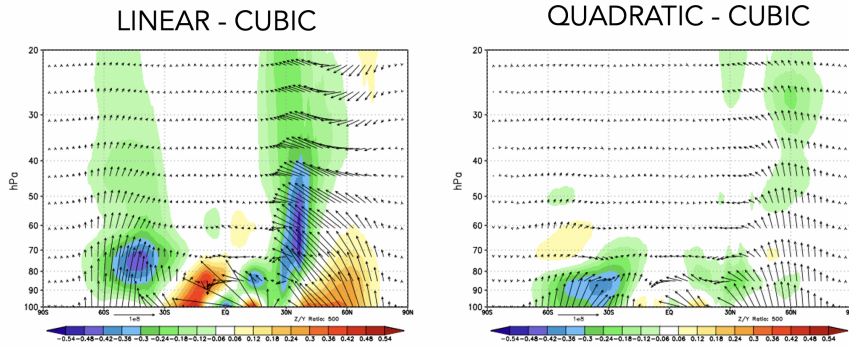
DJF Climatological Mean Eliassen-Palm Flux Divergence ($\nabla \cdot \mathbf{F}$)

Figure 9. Colors shown anomalies in the DJF climatological mean Eliassen-Palm (EP) flux divergence in the LINEAR (left) and QUADRATIC (right) experiments, relative to the CUBIC model experiment. Arrows denote anomalies in the vertical and meridional EP flux vectors.

465 Structurally, the increase in zonal wind strength over northern extratropical mid-
 466 latitudes is reflective of a poleward shift in the zonal winds as the critical latitude, i.e.
 467 where the zonal wind is zero, shifts northward in the QUADRATIC and, especially, LIN-
 468 EAR integrations, relative to the CUBIC experiment (Figure 11). Since stationary waves
 469 only propagate in westerly zonal flow, the latitude where zonal flow is zero acts a bound-
 470 ary for wave propagation (Hardiman et al. (2014)). As a result, this shift in critical lat-
 471 itude results in enhanced wave propagation in that region.

472 Figures 10 and 11 highlight how the changes in zonal winds in the LINEAR and
 473 QUADRATIC experiments reflect a degradation in model skill, relative to MERRA-2,
 474 throughout the entire stratosphere. The changes in upwelling, mean age, chemical trace
 475 gases and zonal winds thus provide an coherent and self-consistent picture suggestive of
 476 a degradation in the representation of the stratospheric circulation since MERRA-2. That
 477 is, an increased bias in the stratospheric northern zonal winds are, via their influence on
 478 wave convergence, compromising changes in the strength of the mean meridional over-
 479 turning circulation and its impact on composition. It is interesting to note that the wind
 480 biases also extend into the troposphere and show degraded skill relative to MERRA-2
 481 in the LINEAR and QUADRATIC experiments (Figure 11). Examination of other fields
 482 (i.e. tropopause biases, Appendix Figure 3) present somewhat more of a nuanced story
 483 that depends more sensitively on latitude and season considered. The improvements in
 484 the zonal winds, however, are most relevant for setting the upwelling characteristics within
 485 the tropical lower stratosphere via their influence on wave propagation into that region.

486 Finally, to better understand why these impacts on the winds have such a conse-
 487 quence for the wave convergence properties within the stratosphere, next we examine the
 488 zonal structure of these biases in the middle stratosphere (Figure 12). This reveals that
 489 the enhanced winds in the LINEAR (and, to a lesser extent, QUADRATIC) integrations
 490 are concentrated over the North Pacific (a similar picture emerges within the troposphere,
 491 not shown). As this region is the primary region dominating the stationary component
 492 of the upward flux of vertical wave activity (Plumb (1985), see their Figure 4) it is per-
 493 haps not surprising that this region is having a profound impact on the mean overturn-
 494 ing circulation. Again, as with the zonal mean wind changes, the increases in wind strength

DJF Climatological Mean Zonal Wind (20°N-60°N)

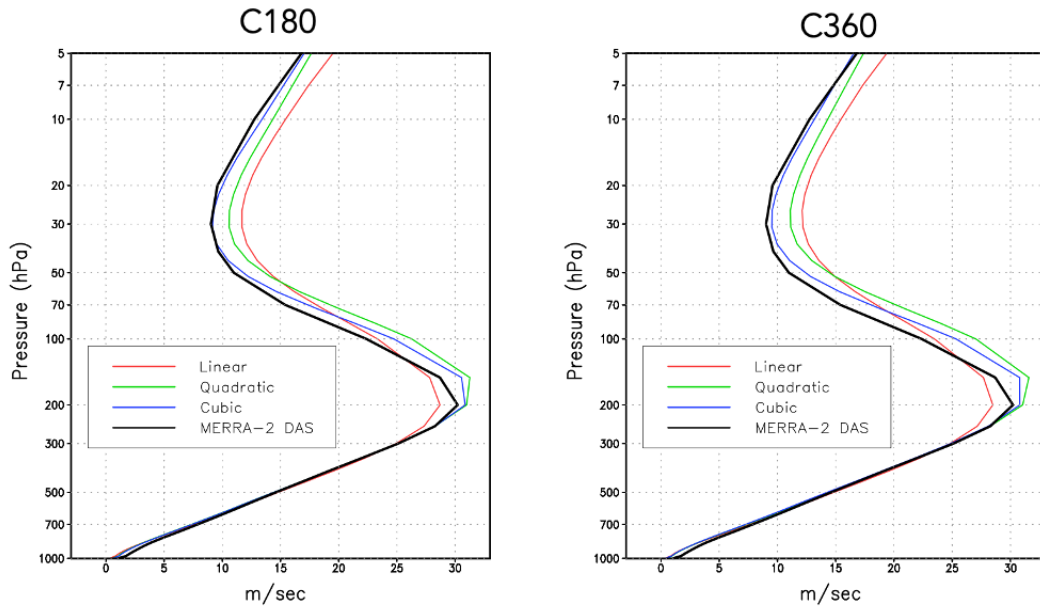


Figure 10. Vertical profiles of the DJF climatological mean zonal mean zonal winds in the LINEAR (red), QUADRATIC (green) and CUBIC (blue) experiments, averaged between 20°N and 40°N. MERRA-2 is shown in the black line. Results for both C180 (left) and C360 (right) experiments are provided.

DJF Climatological Zonal Mean Zonal Wind Anomalies Relative to MERRA-2

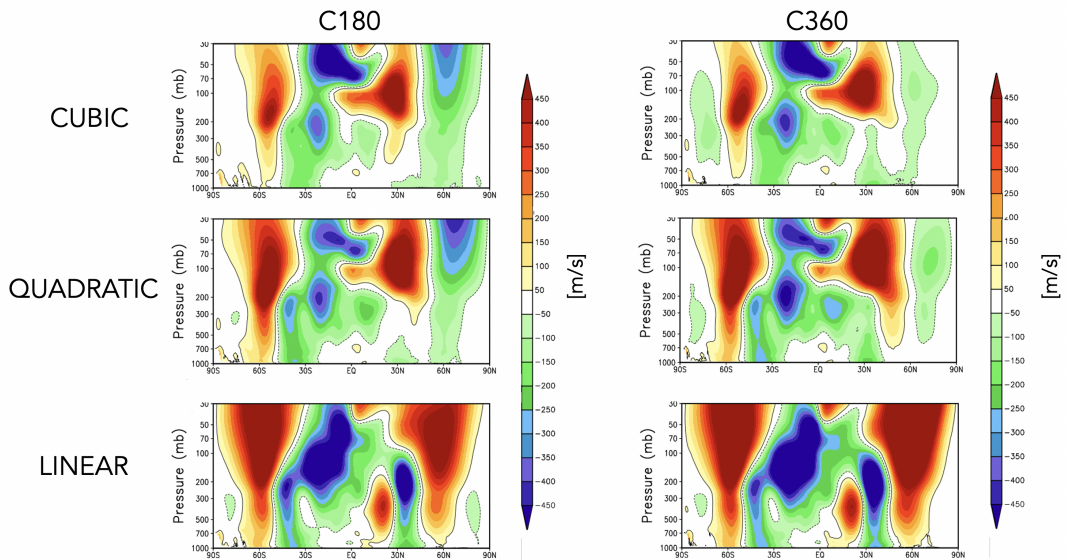


Figure 11. Colors shown anomalies in the DJF climatological mean zonal mean zonal winds in the CUBIC (top), QUADRATIC (middle) and LINEAR (bottom) experiments, relative to MERRA-2. Results for both C180 (left) and C360 (right) experiments are provided.

DJF Climatological 30 hPa Zonal Wind Anomalies Relative to MERRA-2

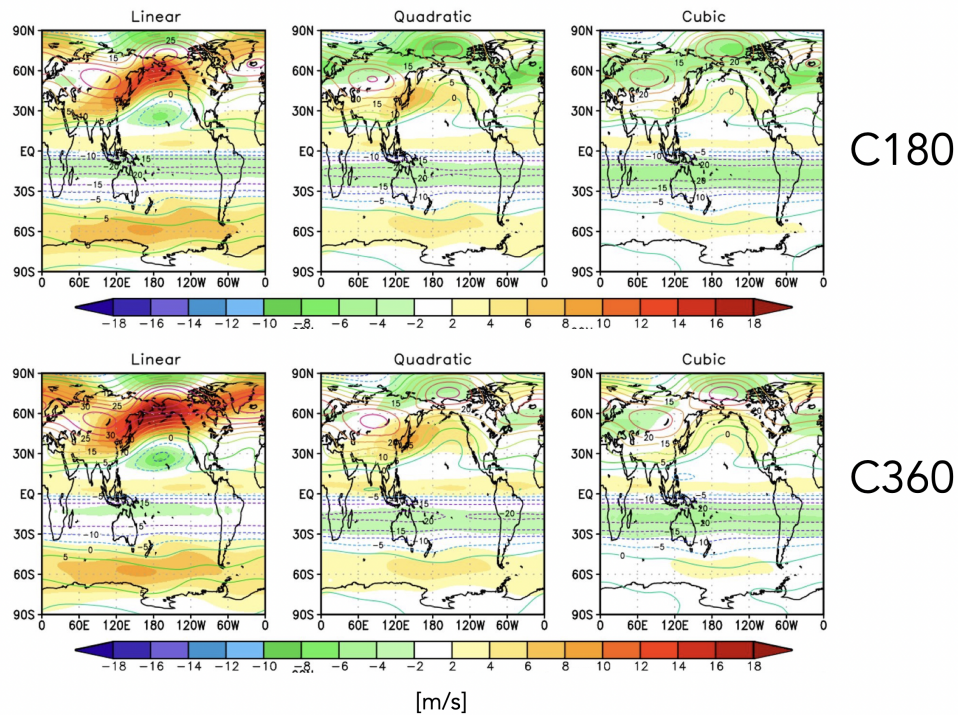


Figure 12. Colors shown anomalies in the DJF climatological mean zonal winds at 30 hPa in the CUBIC (right), QUADRATIC (middle) and LINEAR (left) experiments, relative to MERRA-2. Results for both C180 (top) and C360 (bottom) experiments are provided.

495 over the North Pacific represent degraded model skill relative to MERRA-2. Note that
 496 comparisons with ERA-5 reveal a similar bias (not shown).

497 **3.2.3 FV REMAP Algorithm: Sensitivity of DAS Analysis State**

498 Up to this point our focus has been on evaluating the various model configurations
 499 via use of 30-year long AMIPs, which are required for deriving the integrated transport
 500 statistics (i.e. age-of-air) that reflect the long timescales relevant to setting the strato-
 501 spheric transport circulation. However, this not only poses practical challenges for model
 502 development purposes (which may be ameliorated, for some variables, through use of EMIPs),
 503 but it is also not obvious how the time-integrated model biases inferred from AMIPs man-
 504 ifest in a data assimilation (DAS) context. To this end, here we briefly comment on im-
 505 plications for the DAS analysis state.

506 In particular, we compare two DAS experiments one mimicking MERRA2 (d46aremp2)
 507 and one mimicking the control configuration (d46actrl) (Table 2, rows 8-9). As in the
 508 previous section, we also consider the robustness of results to changes in horizontal res-
 509 olution.

510 **Need to write when receive Amal's new figure (current Figure 13 is only a place-**
 511 **holder).**

PLACEHOLDER

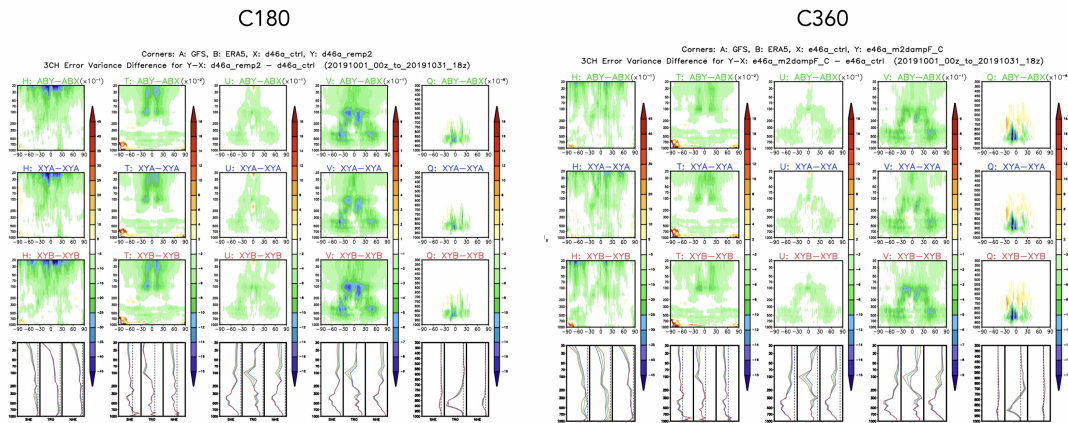


Figure 13. Need to fill in when figure has been decided.

4 Conclusions

Here we have presented an analysis aimed at understanding changes in the representation of the stratospheric circulation occurring in several model configurations of GEOS-5 moving from MERRA-2 to more recent candidate systems for GEOS-R21C. Through the use of targeted model experiments oriented at disentangling various model development updates, we have identified a key role played by changes in the handling of the remapping algorithm within the model's finite-volume dynamical core. Our key results are as follows:

#1. The stratospheric mean age-of-air in GEOS-5 is sensitive to the degree of the interpolation scheme that is used to calculate layer-mean values of total energy, u , v and tracers. Different handling of details in the vertical remapping algorithm (REMAP Option 1 vs. 2) result in mid-stratospheric (50 hPa) age-of-air differences of ~ 1 year over high latitudes, or about 30% climatological mean values.

#2. The age-of-air sensitivities reflect, to first order, changes in the strength of tropical upwelling associated with the Brewer-Dobson circulation which are in turn driven by changes in EP flux convergence over northern midlatitudes. Changes in wave convergence reflect shifts in (critical lines of) wave propagation that originate in the troposphere over the Pacific Ocean, a region of strong upward wave activity.

#3. The degradation of age-of-air, upwelling and zonal wind climate statistics manifest in AMIPs, also translate to degradations in the DAS analysis states of a broad range of variables. Both DAS- and AMIP-based findings are not sensitive to horizontal resolution.

Although our focus here has been on the transport circulation, motivating our use of tracer-independent metrics like the age-of-air, our results have clear implications for constituent transport in GEOS-R21C. In particular, we showed that the increased age-of-air biases correspond to increased biases in the representations of CH_4 and N_2O moving from the CCM1 Phase 1 to Phase 2 model configuration. This comports with well-known correlations between the mean age and stratospheric trace gases, reinforcing the fact that model transport inaccuracies continue to significantly affect simulations of important long-lived chemical species in the stratosphere (Hall et al. (1999)).

542 Our results highlight the key role played by model numerics in transport (e.g., Rood
543 (1987)). The sensitivities in the age-of-air documented herein are also consistent in spirit
544 with the findings in Gupta et al. (2020) who showed significant age differences occurring
545 between spectral versus finite-volume numerics. Our results, however, suggest that there
546 remain large sensitivities even within a given (FV) dynamical core. Furthermore, we also
547 show that that statistics derived from long AMIPS also manifest within a data assim-
548 ilation context, which raises important questions as to the degree to which model biases
549 can be ameliorated through assimilation of observations.

550 Looking forward, our findings support and build on the recommendation proposed
551 in Gupta et al. (2020) for the construction of dynamical core benchmark tests aimed at
552 determining how underlying AGCM numerics and resolution impact climatological trans-
553 port properties. In particular, in addition to the age-of-air, the authors propose a range
554 of stratospheric circulation diagnostics that should be evaluated including the zonal mean
555 zonal winds, eddy temperature variance and zonal spectra of eddy kinetic energy. Our
556 analysis reveals an important role to be played by the climatological zonal mean wind
557 structure as it impacts wave convergence over midlatitudes; we therefore also recommend
558 explicit consideration of the Eliassen Palm flux convergence and tropical upwelling (w^*)
559 fields as they may be crucial for interpreting age-of-air changes.

560 One somewhat incidental – but practical - result from our analysis is that the statis-
561 tics of $\nabla \cdot \mathbf{F}$ and w^* are well approximated by ensembles of so-called EMIP integrations.
562 As these are substantially easier to run than AMIPs these could provide a “first pass”
563 when evaluating new proposed model development changes, without the immediate need
564 to integrate AMIP-style experiments. We emphasize, however, that this statement should
565 only apply to a first stage in model development as the age-of-air will reflect the time
566 integrated impacts of both advection and mixing.

567 Finally, we conclude by noting that, while we have focused on sensitivities within
568 the FV remapping algorithm, our results have highlighted important sensitivities to changes
569 in radiation and, to a lesser extent, changes in parameterized convection. Though not
570 the dominant drivers of the age-of-air changes exhibited here, the former could poten-
571 tially both directly influence the age through changes in thermal structure and indirectly
572 influence the age by modified wave propagation and/or generation in the troposphere.
573 Future work will focus on examining these influences.

PLACEHOLDER

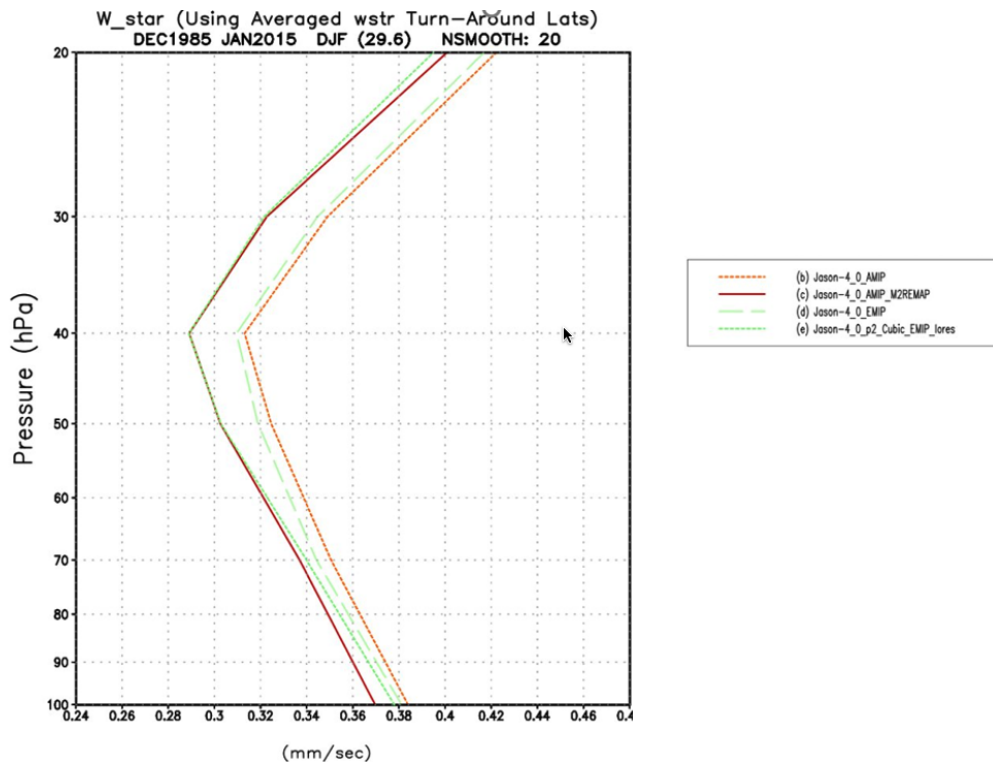


Figure A1. The DJF climatological mean vertical residual mean velocity, w^* , averaged between the turnaround latitudes for the CTRL experiment (Table 2, row 1). Results based on a 30-year-long AMIP experiment (dotted orange line) and a 30-member ensemble of three-month-long EMIP experiments (dashed green line) are shown.

574 **Appendix A Appendix Figures**575 **Open Research Section**

576 TBD

577 **Acknowledgments**

578 TBD

579 **References**

- 580 Abalos, M., Calvo, N., Benito-Barca, S., Garny, H., Hardiman, S. C., Lin, P., . . .
581 others (2021). The brewer–dobson circulation in cmip6. *Atmospheric Chem-*
582 *istry and Physics*, 21(17), 13571–13591.
- 583 Abalos, M., Orbe, C., Kinnison, D. E., Plummer, D., Oman, L. D., Jöckel, P., . . .
584 others (2020). Future trends in stratosphere-to-troposphere transport in ccmi

PLACEHOLDER

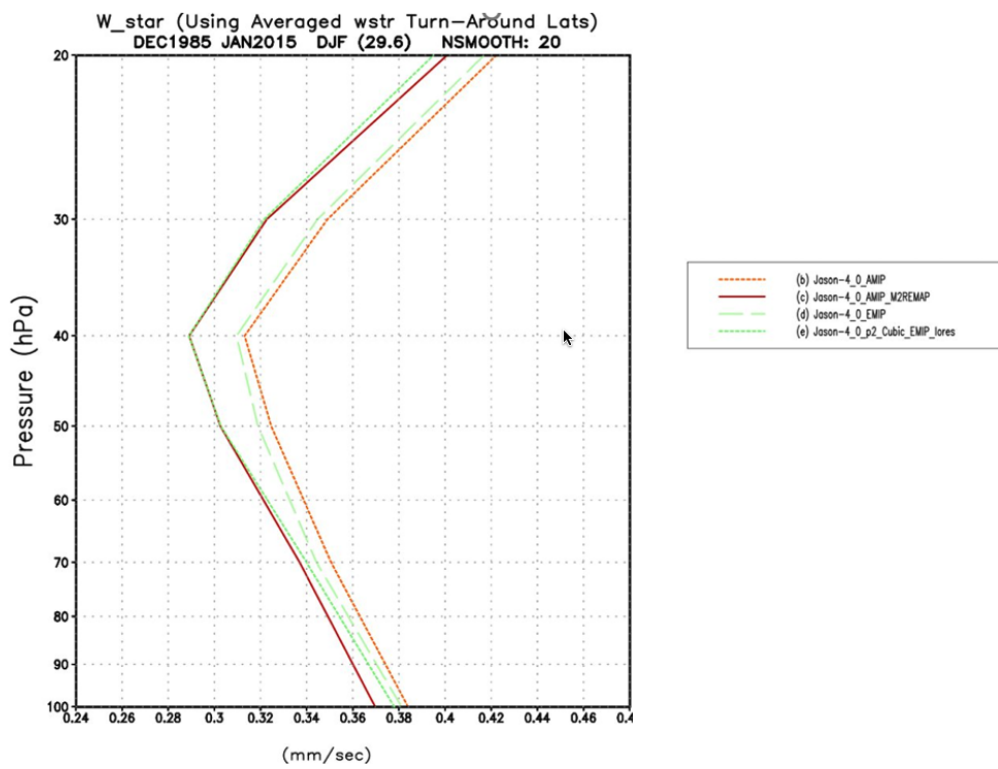


Figure A2. PLACEHOLDER

C180 EMIP 30-yr DJF Climatology (Dec 1985 – Feb 2015)

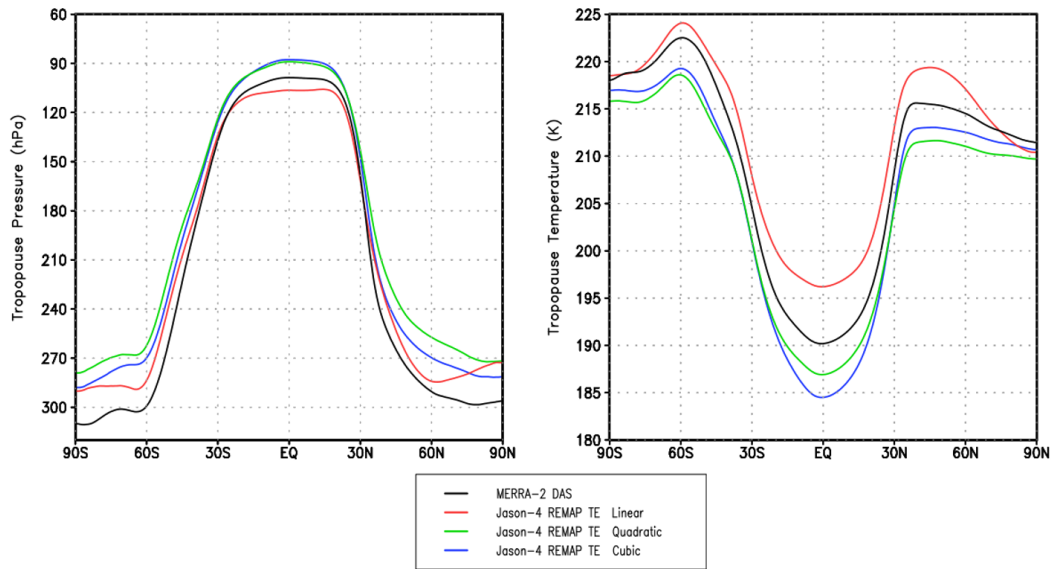


Figure A3. The DJF climatological mean tropopause pressure (left) and temperature (right) in the CUBIC (blue), QUADRATIC (green and LINEAR (red) experiments. MERRA-2 is shown in black. Results are presented for the C180 experiments.

- 585 models. *Atmospheric Chemistry and Physics*, 20(11), 6883–6901.
- 586 Abalos, M., Randel, W. J., Kinnison, D. E., & Garcia, R. R. (2017). Using the artificial tracer e90 to examine present and future utls tracer transport in waccm.
- 587 *Journal of the Atmospheric Sciences*, 74(10), 3383–3403.
- 588 Andrews, D., Holton, J., & Leovy, C. (1987). Middle Atmosphere Dynamics. *Academic Press*, 60, 489. doi: 10.1175/1520-0469(2003)060(0103:CEOAL)2.0.CO;2
- 589 Arnold, N. P., Putman, W. M., & Freitas, S. R. (2020). Impact of resolution and
- 590 parameterized convection on the diurnal cycle of precipitation in a global
- 591 nonhydrostatic model. *Journal of the Meteorological Society of Japan. Ser. II.*
- 592 Boering, K. A., Wofsy, S., Daube, B., Schneider, H., Loewenstein, M., Podolske, J.,
- 593 & Conway, T. (1996). Stratospheric mean ages and transport rates from obser-
- 594 vations of carbon dioxide and nitrous oxide. *Science*, 274(5291), 1340–1343.
- 595 Butchart, N., Cionni, I., Eyring, V., Shepherd, T., Waugh, D., Akiyoshi, H., ...
- 596 others (2010). Chemistry–climate model simulations of twenty-first century
- 597 stratospheric climate and circulation changes. *Journal of Climate*, 23(20),
- 598 5349–5374.
- 599 Chiodo, G., & Polvani, L. M. (2019). The response of the ozone layer to quadrupled
- 600 co 2 concentrations: Implications for climate. *Journal of climate*, 32(22),
- 601 7629–7642.
- 602 Chou, M.-D. (1990). Parameterizations for the absorption of solar radiation by o
- 603 2 and co 2 with application to climate studies. *Journal of Climate*, 3(2), 209–
- 604 217.
- 605 Chou, M.-D. (1992). A solar radiation model for use in climate studies. *Journal of*
- 606 *Atmospheric Sciences*, 49(9), 762–772.
- 607 Chou, M.-D., & Suarez, M. J. (1994). An efficient thermal infrared radiation param-

- 611 eterization for use in general circulation models.
- 612 Davis, N. A., Callaghan, P., Simpson, I. R., & Tilmes, S. (2022). Specified dynamics
613 scheme impacts on wave-mean flow dynamics, convection, and tracer transport
614 in cesm2 (waccm6). *Atmospheric Chemistry and Physics*, *22*(1), 197–214.
- 615 Dietmüller, S., Eichinger, R., Garny, H., Birner, T., Boenisch, H., Pitari, G., . . . oth-
616 ers (2018). Quantifying the effect of mixing on the mean age of air in ccmval-2
617 and ccmi-1 models. *Atmospheric Chemistry and Physics*, *18*(9), 6699–6720.
- 618 Eichinger, R., Garny, H., Šácha, P., Danker, J., Dietmüller, S., & Oberländer-Hayn,
619 S. (2020). Effects of missing gravity waves on stratospheric dynamics; part 1:
620 climatology. *Climate Dynamics*, *54*(5), 3165–3183.
- 621 Eluszkiewicz, J., Hemler, R. S., Mahlman, J. D., Bruhwiler, L., & Takacs, L. L.
622 (2000). Sensitivity of age-of-air calculations to the choice of advection scheme.
623 *Journal of the atmospheric sciences*, *57*(19), 3185–3201.
- 624 Engel, A., Möbius, T., Böenisch, H., Schmidt, U., Heinz, R., Levin, I., . . . others
625 (2009). Age of stratospheric air unchanged within uncertainties over the past
626 30 years. *Nature Geoscience*, *2*(1), 28–31.
- 627 Eyring, V., Lamarque, J.-F., Hess, P., Arfeuille, F., Bowman, K., Chipperfield,
628 M. P., . . . others (2013). Overview of igac/sparc chemistry-climate model
629 initiative (ccmi) community simulations in support of upcoming ozone and
630 climate assessments. *SPARC newsletter*, *40*(January), 48–66.
- 631 Freitas, S. R., Grell, G. A., Molod, A., Thompson, M. A., Putman, W. M., Santos e
632 Silva, C. M., & Souza, E. P. (2018). Assessing the grell-freitas convection
633 parameterization in the nasa geos modeling system. *Journal of Advances in*
634 *Modeling Earth Systems*, *10*(6), 1266–1289.
- 635 Freitas, S. R., Putman, W. M., Arnold, N. P., Adams, D. K., & Grell, G. A. (2020).
636 Cascading toward a kilometer-scale gcm: Impacts of a scale-aware convection
637 parameterization in the goddard earth observing system gcm. *Geophysical*
638 *Research Letters*, *47*(17), e2020GL087682.
- 639 Gelaro, R., McCarty, W., Suárez, M. J., Todling, R., Molod, A., Takacs, L., . . .
640 others (2017). The modern-era retrospective analysis for research and applica-
641 tions, version 2 (merra-2). *Journal of climate*, *30*(14), 5419–5454.
- 642 Grell, G. A., & Freitas, S. R. (2014). A scale and aerosol aware stochastic convective
643 parameterization for weather and air quality modeling. *Atmospheric Chemistry*
644 *and Physics*, *14*(10), 5233–5250.
- 645 Grooß, J.-U., & Russell III, J. M. (2005). A stratospheric climatology for o₃, h₂
646 o, ch₄, no_x, hcl and hf derived from haloe measurements. *Atmospheric chem-*
647 *istry and physics*, *5*(10), 2797–2807.
- 648 Gupta, A., Gerber, E. P., & Lauritzen, P. H. (2020). Numerical impacts on tracer
649 transport: A proposed intercomparison test of atmospheric general circula-
650 tion models. *Quarterly Journal of the Royal Meteorological Society*, *146*(733),
651 3937–3964.
- 652 Hall, T. M., & Plumb, R. A. (1994). Age as a diagnostic of stratospheric transport.
653 *Journal of Geophysical Research: Atmospheres*, *99*(D1), 1059–1070.
- 654 Hall, T. M., Waugh, D. W., Boering, K. A., & Plumb, R. A. (1999). Evaluation
655 of transport in stratospheric models. *Journal of Geophysical Research: Atmo-*
656 *spheres*, *104*(D15), 18815–18839.
- 657 Hardiman, S. C., Butchart, N., & Calvo, N. (2014). The morphology of the brewer-
658 dobson circulation and its response to climate change in cmip5 simulations.
659 *Quarterly Journal of the Royal Meteorological Society*, *140*(683), 1958–1965.
- 660 Haynes, P., McIntyre, M., Shepherd, T., Marks, C., & Shine, K. P. (1991). On the
661 “downward control” of extratropical diabatic circulations by eddy-induced
662 mean zonal forces. *Journal of the Atmospheric Sciences*, *48*(4), 651–678.
- 663 Hegglin, M. I., Brunner, D., Peter, T., Hoor, P., Fischer, H., Staehelin, J., . . . Weers,
664 U. (2006). Measurements of no, no_y, n₂o, and o₃ during spurt: implica-
665 tions for transport and chemistry in the lowermost stratosphere. *Atmospheric*

- 666 *chemistry and physics*, 6(5), 1331–1350.
- 667 Holton, J. R., Haynes, P. H., McIntyre, M. E., Douglass, A. R., Rood, R. B., & Pfister,
668 L. (1995). Stratosphere-troposphere exchange. *Reviews of geophysics*,
669 33(4), 403–439.
- 670 Holzer, M., & Hall, T. M. (2000). Transit-time and tracer-age distributions in geo-
671 physical flows. *Journal of the atmospheric sciences*, 57(21), 3539–3558.
- 672 Iacono, M. J., Delamere, J. S., Mlawer, E. J., Shephard, M. W., Clough, S. A., &
673 Collins, W. D. (2008). Radiative forcing by long-lived greenhouse gases:
674 Calculations with the aer radiative transfer models. *Journal of Geophysical*
675 *Research: Atmospheres*, 113(D13).
- 676 Ivy, D. J., Solomon, S., Calvo, N., & Thompson, D. W. (2017). Observed connec-
677 tions of arctic stratospheric ozone extremes to northern hemisphere surface
678 climate. *Environmental Research Letters*, 12(2), 024004.
- 679 Kouatchou, J., Molod, A., Nielsen, J., Auer, B., Putman, W., & Clune, T. (2015).
680 *Geos-5 chemistry transport model user’s guide* (Tech. Rep.).
- 681 Legras, B., Pissot, I., Berthet, G., & Lefèvre, F. (2004). Variability of the lagrangian
682 turbulent diffusivity in the lower stratosphere. *Atmospheric Chemistry and*
683 *Physics Discussions*, 4(6), 8285–8325.
- 684 Molod, A., Takacs, L., Suarez, M., & Bacmeister, J. (2015). Development of the
685 geos-5 atmospheric general circulation model: Evolution from merra to merra2.
686 *Geoscientific Model Development*, 8(5), 1339–1356.
- 687 Monge-Sanz, B., Chipperfield, M., Simmons, A., & Uppala, S. (2007). Mean age of
688 air and transport in a ctm: Comparison of different ecmwf analyses. *Geophys-*
689 *ical Research Letters*, 34(4).
- 690 Monge-Sanz, B. M., Bozzo, A., Byrne, N., Chipperfield, M. P., Diamantakis, M.,
691 Flemming, J., ... others (2022). A stratospheric prognostic ozone for seam-
692 less earth system models: performance, impacts and future. *Atmospheric*
693 *Chemistry and Physics*, 22(7), 4277–4302.
- 694 Morgenstern, O., & Carver, G. D. (2001). Comparison of cross-tropopause transport
695 and ozone in the upper troposphere and lower stratosphere region. *Journal of*
696 *Geophysical Research: Atmospheres*, 106(D10), 10205–10221.
- 697 Neu, J., Strahan, S., Braesicke, P., Douglass, A., Huck, P., Oman, L., ... Tegtmeier,
698 S. (2010). Sparc ccmval (2010), sparc report on the evaluation of chemistry-
699 climate models: Chapter 5: Transport. SPARC.
- 700 Neu, J. L., & Plumb, R. A. (1999). Age of air in a “leaky pipe” model of strato-
701 spheric transport. *Journal of Geophysical Research: Atmospheres*, 104(D16),
702 19243–19255.
- 703 Oehrlein, J., Chiodo, G., & Polvani, L. M. (2020). The effect of interactive ozone
704 chemistry on weak and strong stratospheric polar vortex events. *Atmospheric*
705 *Chemistry and Physics*, 20(17), 10531–10544.
- 706 Orbe, C., Oman, L. D., Strahan, S. E., Waugh, D. W., Pawson, S., Takacs, L. L., &
707 Molod, A. M. (2017). Large-scale atmospheric transport in geos replay simula-
708 tions. *Journal of Advances in Modeling Earth Systems*, 9(7), 2545–2560.
- 709 Orbe, C., Rind, D., Jonas, J., Nazarenko, L., Faluvegi, G., Murray, L. T., ... oth-
710 ers (2020). Giss model e2. 2: A climate model optimized for the middle
711 atmosphere—2. validation of large-scale transport and evaluation of cli-
712 mate response. *Journal of Geophysical Research: Atmospheres*, 125(24),
713 e2020JD033151.
- 714 Orbe, C., Yang, H., Waugh, D. W., Zeng, G., Morgenstern, O., Kinnison, D. E., ...
715 others (2018). Large-scale tropospheric transport in the chemistry-climate
716 model initiative (ccmi) simulations. *Atmospheric Chemistry and Physics*,
717 18(10), 7217–7235.
- 718 Pan, L. L., Wei, J., Kinnison, D., Garcia, R., Wuebbles, D., & Brasseur, G. P.
719 (2007). A set of diagnostics for evaluating chemistry-climate models in the ex-
720 tratropical tropopause region. *Journal of Geophysical Research: Atmospheres*,

- 721 112(D9).
- 722 Pawson, S., Stajner, I., Kawa, S. R., Hayashi, H., Tan, W.-W., Nielsen, J. E., ...
- 723 Livesey, N. J. (2007). Stratospheric transport using 6-h-averaged winds from
- 724 a data assimilation system. *Journal of Geophysical Research: Atmospheres*,
- 725 112(D23).
- 726 Plumb, R. A. (1985). On the three-dimensional propagation of stationary waves.
- 727 *Journal of Atmospheric Sciences*, 42(3), 217–229.
- 728 Plumb, R. A. (1996). A “tropical pipe” model of stratospheric transport. *Journal of*
- 729 *Geophysical Research: Atmospheres*, 101(D2), 3957–3972.
- 730 Plumb, R. A. (2002). Stratospheric transport. *Journal of the Meteorological Society*
- 731 *of Japan. Ser. II*, 80(4B), 793–809.
- 732 Polvani, L. M., Waugh, D. W., Correa, G. J., & Son, S.-W. (2011). Stratospheric
- 733 ozone depletion: The main driver of twentieth-century atmospheric circulation
- 734 changes in the southern hemisphere. *Journal of Climate*, 24(3), 795–812.
- 735 Prather, M. J., Zhu, X., Tang, Q., Hsu, J., & Neu, J. L. (2011). An atmospheric
- 736 chemist in search of the tropopause. *Journal of Geophysical Research: Atmo-*
- 737 *spheres*, 116(D4).
- 738 Rood, R. B. (1987). Numerical advection algorithms and their role in atmospheric
- 739 transport and chemistry models. *Reviews of geophysics*, 25(1), 71–100.
- 740 Rosenlof, K. H. (1995). Seasonal cycle of the residual mean meridional circulation
- 741 in the stratosphere. *Journal of Geophysical Research: Atmospheres*, 100(D3),
- 742 5173–5191.
- 743 Son, S.-W., Tandon, N. F., Polvani, L. M., & Waugh, D. W. (2009). Ozone hole and
- 744 southern hemisphere climate change. *Geophysical Research Letters*, 36(15).
- 745 Strahan, S., Douglass, A., & Newman, P. (2013). The contributions of chemistry
- 746 and transport to low arctic ozone in march 2011 derived from aura mls obser-
- 747 vations. *Journal of Geophysical Research: Atmospheres*, 118(3), 1563–1576.
- 748 Thiele, G., & Sarmiento, J. (1990). Tracer dating and ocean ventilation. *Journal of*
- 749 *Geophysical Research: Oceans*, 95(C6), 9377–9391.
- 750 Waugh, D., & Hall, T. (2002). Age of stratospheric air: Theory, observations, and
- 751 models. *Reviews of Geophysics*, 40(4), 1–1.